

Hybridized method of pseudopotential lattice Boltzmann and cubic-plus-association equation of state assesses thermodynamic characteristics of associating fluids

Mohammad Bagher Asadi and Sohrab Zendehboudi*

Faculty of Engineering and Applied Science, Memorial University, St. John's, NL, Canada A1B 3X5



(Received 24 January 2019; published 4 October 2019)

It is crucial to properly describe the associating fluids in terms of phase equilibrium behaviors, which are needed for design, operation, and optimization of various chemical and energy processes. Pseudopotential lattice Boltzmann method (LBM) appears to be a reliable and efficient approach to study thermodynamic behaviors and phase transition of complex fluid systems. However, when cubic equations of state (EOSs) are incorporated into single-component multiphase LBM, simulation results are not well matched with experimental data. This study presents the utilization of cubic-plus-association (CPA) EOS in the LBM structure to obtain more accurate modeling results for associating fluids. An approach based on the global search optimization algorithm is introduced to find the optimal association parameters of CPA EOS for water and primary alcohols in the lattice units. The thermodynamic consistency is verified by the Maxwell construction and is also improved by the forcing scheme of [Q. Li, K. H. Luo, and X. J. Li, *Phys. Rev. E* **86**, 016709 (2012)]. The spurious velocity is reduced with increasing isotropy in the gradient operator. Furthermore, an extended version of CPA EOS is introduced, which increases the system stability at low reduced temperatures. There is a very good match between the LBM results and experimental data, confirming the reliability of the model developed in the present study. The introduced approach has potential to be employed for simulating transport phenomena and interfacial characteristics of associating fluids in porous systems.

DOI: [10.1103/PhysRevE.100.043302](https://doi.org/10.1103/PhysRevE.100.043302)

I. INTRODUCTION

Cubic equations of state (EOSs) such as Peng-Robinson (PR) [3] and Soave-Redlich-Kwong (SRK) [4] have been extensively used to model thermodynamic behaviors of hydrocarbon and nonhydrocarbon fluids, due to their simplicity and accuracy. Unusual thermodynamic behaviors are generally observed for fluids with hydrogen bonds while employing cubic EOSs [5]. Water is an associating component, which commonly exists in various mixtures such as petroleum reservoir fluids as a connate water and injection fluid. Taking another example, asphaltene molecules as a group of complex components may form aggregates due to the association forces. The bonding among polar components is stronger than physical interactions. Therefore, the associating fluids may not be fully described by cubic EOSs [6]. The cubic-plus-association (CPA) EOS was introduced by Kontogeorgis *et al.* [7] to consider the association effects in associating fluids. The CPA EOS has both physical and association parts so that it turns into a cubic EOS in the absence of associating components. In fact, the additional term in the CPA EOS exhibits the association impact, which is originated from the Wertheim theory. This is the same association expression that is utilized in the statistical association fluid theory (SAFT) EOS. The CPA EOS has been broadly employed to study the thermodynamic conditions of complex reservoir fluids. For example, Li and Firoozabadi introduced a generalized strategy based on the CPA EOS to determine the amount of asphaltene

precipitation [8–10]. A general review on the CPA EOS can be found in the works conducted by Kontogeorgis *et al.* [5,11].

On the basis of the Reynolds-averaged Navier-Stokes (RANS) equations, the computational fluid dynamics methods have been successfully implemented in several mechanical and chemical engineering cases. The applications of large eddy simulation (LES) and direct numerical simulation (DNS) approaches have been considerably increased due to the strong computational capability of supercomputers. However, these methods are based on the continuum assumption. Hence, they might not be able to capture the (micro-)mesoscale physics of targeted processes and/or phenomena. On the other hand, some basic particle-based techniques have been introduced to provide better physical insights of multiphase flow systems. For instance, quantum molecular simulation (QMS), molecular-dynamic simulation (MD), direct simulation Monte Carlo (DSMC), and dissipative particle dynamics (DPD) appear to be efficient strategies to explore the molecular interactions and forces as well as detailed mechanisms of phenomena occurring at (micro-)mesoscales. However, these tools dictate high computational costs, which may make them unfeasible and/or uneconomical in practical scenarios.

Figure 1 provides some information such as computational costs, scale, and physical insights corresponding to the experimental and modeling techniques with focus on flow in porous media. The flow regime is also categorized based on the Knudsen number. In general, the modeling techniques are divided into the continuum based and particle-dynamic based modeling approaches. Additionally, the experimental techniques and their scale are demonstrated. According to

*Corresponding author: szendehboudi@mun.ca

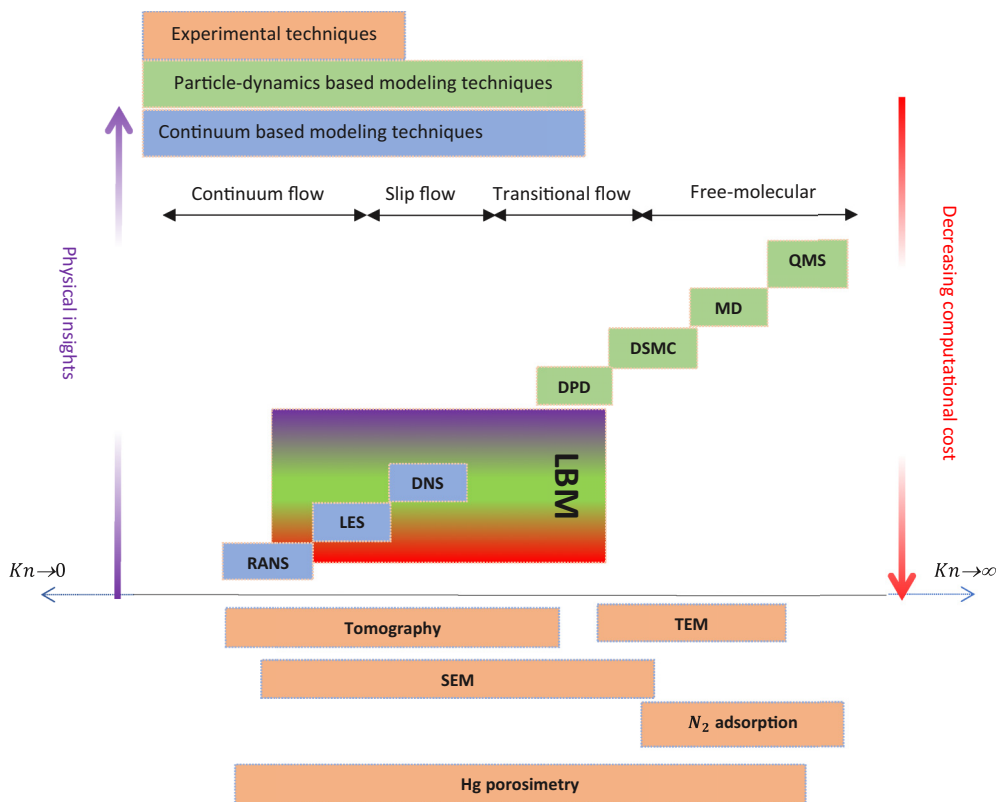


FIG. 1. Experimental and modeling approaches to investigate transport phenomena in porous media, modified after Refs. [1,2]. (QMS is the quantum molecular simulation; MD is the molecular-dynamic simulation; DSMC refers to the direct simulation Monte Carlo; DPD is the dissipative particle dynamics; LBM refers to the lattice Boltzmann method; DNS is the direct numerical simulation; LES represents the large eddy simulation; RANS refers to the Reynolds-averaged Navier-Stokes; TEM is the transmission electron microscopy; and SEM denotes the scanning electron microscope.) (The scale of methods is shown approximately and there are overlaps between different methods.)

Fig. 1, as the capability of modeling techniques is increased, the computational costs will increase.

The lattice Boltzmann method (LBM) as a mesoscale technique was introduced in the 1980s [12,13]. The LBM is recognized as a strategy based on a particle picture to obtain the macroscopic properties of fluids and processes [14]. Over the past three decades, LBM has been used in a variety of engineering and science problems such as single-phase flow [15–17], multiphase flow [1,18–20], phase-change heat transfer [1,21], and turbulent regime in various transport phenomena [22–26]. This method can be also utilized as a tool to solve nonlinear partial differential equations [27–32].

Multiphase (multicomponent) interfaces play a crucial role in several soft matters and complex fluids. Interfaces are deformable and not known *a priori*. Therefore, different techniques have been proposed to study the dynamics of interfaces [31]. The methodologies fall into two main categories [33]. The first category is the interface-tracking methods such as the front-tracking approach [34], which tracks the interface by marking a cluster of points. The second class is the interface-capturing techniques including the level set method [35], volume of fluid method [36], and phase-filled approach [37] that capture the interface by evaluating an order parameter.

Several multiphase LBM approaches have been developed during the past three decades. The color-gradient method [38,39], free-energy model [40], interface tracking model

(also known as He-Chen-Zhang (HCZ) technique) [41], and pseudopotential [42] are the most common multiphase LBMs. More details about various versions of LBM are provided in the literature [14,19,20,43–47]. Among different types of LBM, the pseudopotential approach (also known as Shan-Chen) has been widely used in some research studies due to its mesoscopic feature and computational simplicity [43–48]. In this approach, the interactions between molecules are represented by a pseudopotential, which is density dependent. Microscopic molecular short-range interactions between different phases are taken into account in this method. Therefore, the interface capturing or explicit interface tracking is not required anymore, which leads to different (unique) features for the pseudopotential model, compared to most other multiphase models [19]. The pseudopotential LBM has some drawbacks. For instance, it suffers from high spurious velocity as the density ratio of two phases is increased near a curved interface. Shan showed that increasing the order of isotropic gradient operator can lower the spurious velocity [49]. The midrange potential can be an alternative to enlarge the interface thickness and to decrease the spurious velocity by considering the nearest- and next-nearest-neighbor interactions [50]. Sbragaglia and Shan proposed a consistent form of the pseudopotential and compared it with the common form of the pseudopotential function available in the literature when a simulation was performed using the eighth order of isotropy [51]. Khajepour *et al.* introduced a

multipseudopotential interaction (MPI) scheme to meet the thermodynamic consistency by determining the interaction strength pseudopotential constants through a trial and error procedure [52]. Later on, Khajepour and Chen mapped the cubic EOS (e.g., SRK and PR) to MPI when the Gou *et al.* forcing scheme was employed [53]. Li *et al.* introduced a new forcing scheme to meet the thermodynamic consistency when the Carnahan-Starling EOS was utilized in the pseudopotential function [54]. The implemented forcing scheme represents the exact Navier-Stokes equations.

Yuan and Schaefer suggested a method of integrating LBM with different EOSs [55]. They evaluated the performance of cubic and noncubic EOSs and determined the maximum density ratio. The coexistence curves of static bubbles, which were simulated by LBM, were compared with the coexistence curves obtained from the Maxwell equal-area construction. Kupershtokh *et al.* obtained a higher density ratio by introducing the exact difference method force scheme [56]. In the Yuan and Schaefer method, different densities in some specific ranges might give the same effective mass, where the physical basis of the original Shan-Chen (SC) pseudopotential LBM may be lost [55]. Zhang and Tian proposed an extra parameter to avoid this problem. However, it leads to a high spurious current and low density ratio and it does not meet the Galilean invariance [57]. Yuan and Schaefer compared the LBM results of different EOSs with the experimental saturated density data of water [55]. An appreciable difference between the LBM results and real data was reported in the liquid phase region. In this study, we aim to increase the LBM accuracy and reliability (or lower the difference between the LBM outputs and experimental data) for associating fluids by filling the knowledge gap described above. For this purpose, CPA EOS is incorporated into the LBM strategy. It should be noted that the computational cost is lower while using the CPA EOS, compared to other EOSs such as perturbed-chain statistical associating-fluid theory (PC-SAFT) that take into account the associating forces. Further highlighting the main contribution of the current study, the parameters of CPA EOS are redefined in the lattice units with the aid of an effective global optimization search method. We also introduce a perturbation, which guarantees the thermodynamic consistency and/or stability of the model within a broad range of thermodynamic conditions, particularly at low temperatures.

The remainder of this paper is organized as follows. First, a review on CPA EOS, LBM, framework of their combination, and the numerical modeling setup are presented in Theory and Methodology. Then, the model limitations (drawbacks) are given in Limitations. The modeling validation, results of numerical runs, and interpretation of the results trends are reported in Results and Discussion. In fact, the method is validated through comparing the simulation results with the Maxwell equal area construction and real data. The thermodynamic consistency is improved by using the Li *et al.* forcing scheme. The reliability of the introduced CPA EOS-LBM is also examined where the experimental data of water and simulation results are compared. By increasing the order of isotropic gradient operator, the method stability at low reduced temperatures is also discussed in this section. Lastly, the main outcomes of the current study are listed in the Conclusions.

II. THEORY AND METHODOLOGY

First, the structure and theory of LBM and CPA EOS are briefly presented in this section. We will then describe the integration of LBM and CPA EOS as well as the setup and required steps in the numerical modeling approach.

A. Fundamentals of LBM

The Boltzmann equation with the collisional term is expressed as follows [58]:

$$\frac{\partial f}{\partial t} + \mathbf{v} \frac{\partial f}{\partial \mathbf{x}} + \frac{\mathbf{F}}{\rho} \frac{\partial f}{\partial \mathbf{x}} = \Omega, \quad (1)$$

where $f(\mathbf{x}, \mathbf{v}, t)$ denotes the particle distribution function; \mathbf{x} refers to the spatial coordination; \mathbf{v} is the particle velocity; t symbolizes the time; ρ represents the fluid density; and \mathbf{F} stands for the force. The parameter Ω on the right-hand side of Eq. (1) represents the collision term, which describes the particle distribution function due to the particle collisions. The velocity space is discretized into a finite set of vectors, $\{e_i\}$, along with the lattice structure in the space. Thus, the distribution density function is discretized $\{f(\mathbf{x}, \mathbf{v})\}$ in the LBM. The lattice Boltzmann equation (LBE) is a nonlinear differential integral equation, which is targeted to be approximated by the LBM from the particle point of view [58]. A common way to simplify the collisional integral term is using a single relaxation time toward a suitable local equilibrium, which is known as Bhatnagar-Gross-Krook (BGK). The LBE can be written in the lattice based on the BGK approximation, as given below [58]:

$$\begin{aligned} & f_i(x + e_i \delta_t, t + \delta_t) - f_i(x, t) \\ &= \frac{\delta_t}{\tau} (f_i^{\text{eq}}(x, t) - f_i(x, t)) + S_i, \quad i = 0, 1, 2, \dots, \end{aligned} \quad (2)$$

in which S_i introduces the forcing source and e_i symbolizes the discrete velocities. The left-hand side of Eq. (2) represents the molecular free-streaming, and the right-hand side of Eq. (2) signifies the time relaxation (due to collisions) toward the local Maxwellian equilibrium f_i^{eq} on a timescale τ [14,43,47,59]. The Maxwellian equilibrium function is truncated at the second order to recover the correct hydrodynamic balance in the isothermal regime as follows:

$$f_i^{\text{eq}} = \omega_i \rho_i \left[1 + \frac{\mathbf{u}_a e_{ia}}{c_s^2} + \frac{\mathbf{u}_a \mathbf{u}_b (e_{ia} e_{ib} - c_s^2 \delta_{ab})}{2c_s^4} \right]. \quad (3)$$

In Eq. (3), $c_s = c/\sqrt{3}$ denotes the speed of sound where $c = \delta_x/\delta_t$. δ_t and δ_x represent the lattice time step and spacing, respectively; δ_{ab} is the Kronecker delta where a and b designate the Cartesian components; \mathbf{u} is the velocity; and the ω_i s symbolize a set of weights, which impose the isotropy of the hydrodynamic equations [14,43,47].

Figure 2 demonstrates up to 16th order of the isotropy and associated weights in a two-dimensional (2D) domain. Grid points indicate a set of velocity fields, and the size and color of points represent the magnitude of weights. The method of calculating the extent of weights for higher orders of isotropy is explained with details in Refs. [50,60]. One can calculate the fluid density ρ and velocity \mathbf{u} from the first and second momenta of density distribution function as given

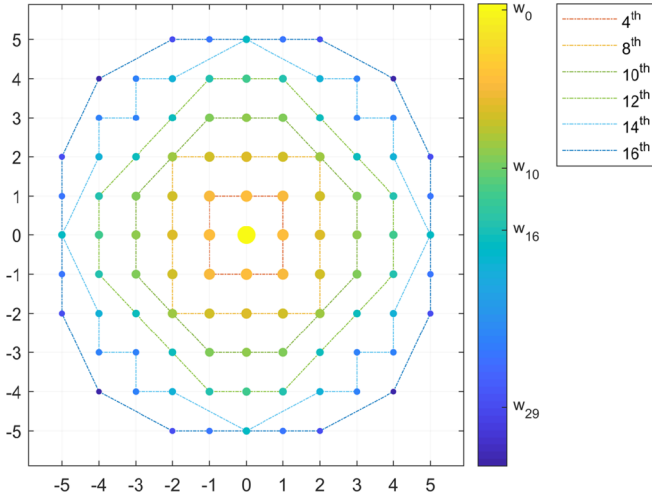


FIG. 2. Different orders of isotropy in 2D domain. The value of weights is determined by the size and color of grids.

below:

$$\rho = \sum_i f_i, \quad (4)$$

$$\rho \mathbf{u} = \sum_i f_i \mathbf{e}_i. \quad (5)$$

B. Pseudopotential interactions in LBM

In the pseudopotential LBM, a mean-field interaction force is employed to mimic the molecular interactions that cause the phase separation. Based on the local fluid density, an interaction potential (ψ) is defined and the interaction force is calculated from the associations/interconnections that lead to the phase separation. In the single-component multiphase (SCMP) LBM, the interparticle force is given as the summation of the pairwise interactions among a particle at a specified lattice site and those at neighboring sites. The interparticle force (F_{int}) can be defined by the following equation:

$$\mathbf{F}_{\text{int}}(x, t) = -G\psi(x, t) \sum_{i=0}^q \omega_i \psi(x + \mathbf{e}_i, t) \mathbf{e}_i, \quad (6)$$

where G is a controlling parameter of the interparticle strength. The interaction force can be expanded through the Taylor series as follows [54]:

$$\mathbf{F}_{\text{int}} = -Gc^2[\psi \nabla \psi + \frac{1}{2}c^2 \psi \nabla (\nabla^2 \psi) + \dots]. \quad (7)$$

To evaluate the mechanical balance at the interface, the pressure tensor should be determined. The following general rule of the force balance is used to obtain the pressure tensor [61]:

$$\Sigma PA = \Sigma_x F. \quad (8)$$

For the one-dimensional interface, the analytical expression of the normal pressure tensor (up to the second-order derivative) is given below [61]:

$$P_n = c_s^2 \rho + \frac{1}{2} Gc^2 \psi^2(\rho) + \frac{Gc^4}{12} \left[\alpha \left(\frac{d\psi}{dn} \right)^2 + \beta \psi \frac{d^2 \psi}{dn^2} \right]. \quad (9)$$

In Eq. (9), $\alpha = 1 - 3e^4$ and $\beta = 1 + 6e^4 e^4$ refers to the fourth-order tensor associated with the weights, as defined below [51]:

$$e^4 = \frac{\omega_1}{2} + 2\omega_2 + 8\omega_4 + 25\omega_5 + 32\omega_8 + \dots \quad (10)$$

The first two diagonal terms of the pressure tensor for the bulk homogeneous phase transition (P_b) are obtained by the nonideal equation of state as follows [55,62]:

$$P_b = c_s^2 \rho + \frac{1}{2} Gc^2 \psi^2(\rho). \quad (11)$$

Therefore, when the density is known, one can calculate the pressure P_b using the CPA EOS where the association forces will be considered. The magnitude of G for the SCMP case is not important as it will be canceled out if the bulk pressure definition is used to determine the pseudopotential function [see Eqs. (6) and (11)]. P_n should be equal to a constant static bulk pressure at the equilibrium, which leads to the following mechanical stability condition [61]:

$$\int_{\rho_g}^{\rho_l} \left(p_0 - \rho c_s^2 - \frac{Gc^2}{2} \psi^2 \right) \frac{\psi'}{\psi^{1+\epsilon}} dp = 0, \quad (12)$$

where $\epsilon = -2\alpha/\beta$; and ρ_l and ρ_g stand for the liquid and gas density, respectively. Li *et al.* proposed the following general forcing scheme [54]:

$$S_i = \omega_i \delta_i \left[\frac{B_a \mathbf{e}_{ia}}{c_s^2} + \frac{C_{ab} (\mathbf{e}_{ia} \mathbf{e}_{ib} - c_s^2 \delta_{ab})}{2c_s^4} \right], \quad (13)$$

where

$$B_a = B_e F_a, \quad C_{ab} = C_e (\mathbf{v}_b F_a + \mathbf{v}_a F_b). \quad (14)$$

B_e and C_e are the constants, which are determined based on the forcing scheme. Li *et al.* introduced a modified velocity v' , which is defined as $v' = v + \sigma' F / (\mathbf{v} \psi^2)$. $\mathbf{v} = (\tau - 0.5)$ stands for the kinematic viscosity and σ' is a constant. In the case of $\sigma' = 0$, the forcing scheme will be reduced to the Guo *et al.* forcing scheme [63]. Hence, implementing Li *et al.*'s forcing approach improves the thermodynamic consistency by adding an extra term to the Navier-Stokes equations, which is not dependent on a local quantity.

C. Cubic-plus-association equation of state

The CPA EOS was introduced by Kontogeorgis *et al.* [7]. This EOS is a combination of a cubic EOS and an association term taken from the Wertheim theory. Originally, the SRK EOS was utilized to describe the physical part of the CPA EOS. Firoozabadi used PR EOS, which is more suitable for thermodynamic modeling of reservoir hydrocarbon fluids [6]. The association term considers the specific site-site interactions due to hydrogen bonding, which appears in two categories, namely, self-association (between the same species) and cross association (between different species). The association term is based on the Wertheim first-order thermodynamic perturbation theory [64]. The system pressure

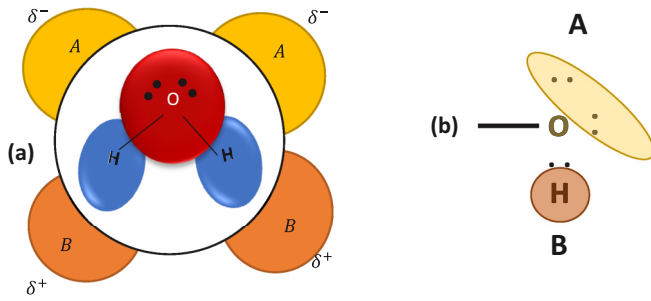


FIG. 3. Simple sketch of (a) a 4C model of water molecules and (b) a 2B model of alcohols.

is represented by the CPA EOS as follows [6]:

$$P = \frac{RT}{v-b} - \frac{a}{v(v+b)+b(v-b)} - \frac{1}{2} \frac{RT}{v} \left(1 - v \frac{\partial \ln g}{\partial v} \right) \sum_i x_i \sum_{A_i} (1 - X_{A_i}),$$

$$i = 1, 2, \dots, n_c, \quad (15)$$

where P refers to the pressure; R is the universal gas constant; T introduces the absolute temperature; v is the molar volume; x denotes the mole fraction; a and b are the attraction and repulsion parameters, respectively; n_c is the number of components; and A_i stands for the active association site. g signifies the hard-sphere radial distribution function and X_{A_i} represents the fraction of site A on component i that does not form association with other sites, as defined below:

$$g \approx \frac{2-\eta}{2(1-\eta)^3} \quad \text{where } \eta = \frac{b}{4v}, \quad (16)$$

$$X_{A_i} = \frac{1}{1 + \sum_{j=1}^{n_c} \sum_{k=A,B,\dots} \rho x_j X_{kj} \Delta_{A_i}^{kj}}, \quad (17)$$

in which $\rho = 1/v$ refers to the density and $\Delta_{A_i}^{kj}$ denotes the self-association strength between sites A and B , as expressed below:

$$\Delta_{A_i}^{kj} = g \left[\exp \left(\frac{\epsilon^{A_i K_i}}{RT} \right) - 1 \right] b_{ij} \beta^{A_i K_i}, \quad (18)$$

$$b_{ij} = \frac{b_i + b_j}{2}, \quad (19)$$

in which $\epsilon^{A_i K_i}$ and $\beta^{A_i K_i}$ introduce the self-association energy and bonding volume parameters, respectively. The association term in Eq. (15) is derived by Michelsen and Hendriks [65] and Hendriks *et al.* [66] to accelerate the computational process. In this study, we use the four-site model (4C) [see panel (a) of Fig. 3], which can generate reliable results for highly hydrogen-bonded substances such as water and glycol [6]. Two A sites are for two oxygen lone pairs and two B sites belong to two hydrogen atoms. According to Huang and Radosz, alcohols can be modeled by two-site scheme (2B): one site for both oxygen lone pairs and one for the hydrogen atom, as depicted in Fig. 3(b) [67].

Based on the literature, the attraction, repulsion parameters, and universal gas constant of cubic EOS are generally kept at $a = 2/49$, $b = 2/21$, and $R = 1$, respectively, in the

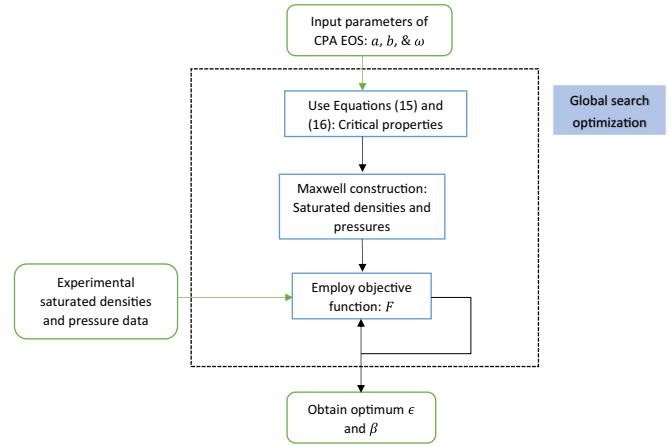


FIG. 4. Work flow for association parameters optimization.

lattice units [52,55]. However, the reduced properties should be the same, while the units are used based on the law of corresponding states. Therefore, the critical properties of the fluid should be updated based on the parameters selected for CPA EOS in the lattice units. For a single-component system, the critical condition is defined as follows [6]:

$$\left. \frac{dP}{dv} \right|_{T=T_c} = 0, \quad (20)$$

and

$$\left. \frac{d^2P}{dv^2} \right|_{T=T_c} = 0, \quad (21)$$

where T_c represents the critical temperature. The explicit form of the first and second derivatives of pressure with respect to volume is obtained by the MAPLE software [68]. The nonlinear system of equations [e.g., Eqs. (20) and (21)] is solved by a MATLAB intrinsic solver (e.g., *fzero*) [69]. Initial guesses are selected based on the roots of the PR EOS [69]. When the critical properties are calculated, the reduced properties can be determined in the lattice units. Thus, it is possible to make a comparison between the experimental data and results of CPA EOS in the lattice units. To determine the association parameters, the experimental data of coexistence densities and saturation pressures are used (see Fig. 4). Coexistence densities are calculated based on the Maxwell construction (see the Appendix). The objective function is defined as follows:

$$F = R_{\text{squared}}(P_r^{\text{sat,exp}}, P_r^{\text{sat,cal}}) + R_{\text{squared}}(\rho_r^{\text{sat,exp}}, \rho_r^{\text{sat,cal}}), \quad (22)$$

in which superscripts sat, exp, and cal denote the saturation condition, experimental data, and calculated results, respectively. A global search optimization is performed to determine the self-association energy (ϵ) and bonding volume (β) parameters.

The global search optimization method is selected to avoid being stuck in probable local optimum points. More details about the global search optimization are provided by Ugray *et al.* [70].

D. Customized CPA EOS

Generally, the highest numerical errors happen within the sharp region of the interfaces, which fall in the unstable branch of the EOS where $(\frac{\partial p}{\partial v})_T > 0$ (e.g., between the spinodal points). The unstable branch can be modified as it is experimentally unapproachable. As Colosqui *et al.* reported, increasing the slope of the unstable branch increases the internal forces towards the liquid side of spinodal and decreases the internal forces towards the vapor zone [71]. However, their proposed piecewise linear EOS had a discontinuity in the first derivative, which is a serious flaw in the numerical discretization [71]. In this study, we propose a perturbation in the unstable branch, which meets the continuity of the first derivative and increases the slope at the same time, as expressed below:

$$P_{\text{Customized}} = P_{\text{CPA}} + \delta P, \quad (23)$$

where δP is a first derivative continuous function as follows:

$$\delta P = \begin{cases} 0 & \text{if } v < v_l \\ \kappa \left(\sin \left(\frac{\pi(v-v_l)}{L_1} + \frac{3\pi}{2} \right) + 1 \right) & \text{if } v_l < v < v_m \\ \kappa \left(\sin \left(\frac{\pi(v-v_l)}{L_2} + \frac{\pi}{2} \right) + 1 \right) & \text{if } v_m < v < v_g \\ 0 & \text{if } v_g < v \end{cases}. \quad (24)$$

In Eq. (24), $v_m = v_g - \alpha(v_g - v_l)$. v_l and v_g stand for the spinodal molar volumes on the liquid and gas sides, respectively. The perturbation is determined by a pair of (α, κ) uniquely.

E. Numerical modeling setup

In this part, the numerical setup is explained, and a convergence condition is introduced. A 100×100 lattice and periodical boundary conditions are used in the numerical bubble tests to study the single-component multiphase LBM. First, a droplet with a radius of $R_{\text{ini}} = 30$ is placed at the center of the domain. Inside the droplet is the liquid phase and the vapor phase is placed outside the droplet. The initial densities are selected based on the Maxwell construction results (see the Appendix). The initial density distribution, $\rho(x, y)$, is defined by the following function:

$$\rho(x, y) = \frac{\rho_{\text{liquid}} + \rho_{\text{gas}}}{2} - \frac{\rho_{\text{liquid}} - \rho_{\text{gas}}}{2} \times \left[\tanh \left(\frac{2\sqrt{(x-x_1)^2 - (y-y_1)^2} - R_0}{w} \right) \right]. \quad (25)$$

In Eq. (25), w introduces the initial interface thickness and R_0 refers to the initial radius. Each test is continued until the steady-state condition is established. The maximum magnitude of spurious velocity, $|u^s|_{\text{max}}$, is selected as the convergence condition to ensure that the steady-state condition is reached. As shown in Fig. 5, the spurious current exhibits high fluctuations. The simulation is conducted at $T_r = 0.8$, where the gas and liquid densities calculated by the Maxwell construction are $\rho_{\text{gas}} = 0.2327$ and $\rho_{\text{liquid}} = 7.3347$, respectively. Yuan and Schaefer performed all runs up to 30 000 time steps when the relative difference of spurious velocity at the time step t and $t - 1000$ is less than 10^{-6} [55].

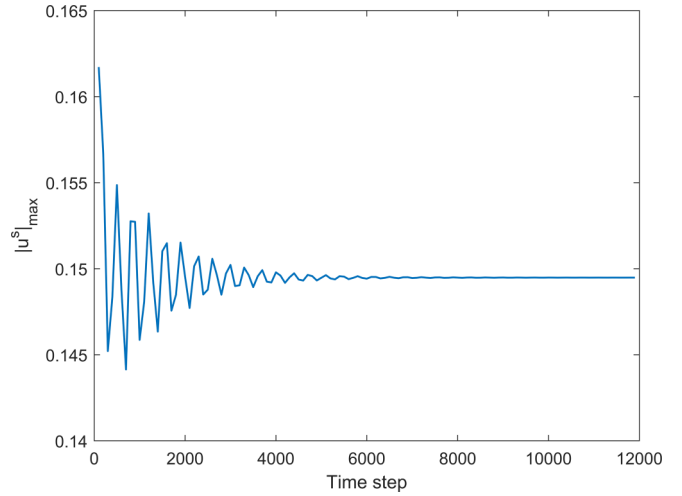


FIG. 5. Fluctuations of the maximum spurious velocity at different time steps.

Huang *et al.* proposed a convergence criterion by evaluating the relative difference of the entire domain velocity between 2000 time steps [72]. In this study, the relative difference of $|u^s_{\text{max}}|$ is calculated every 100 time steps to avoid unnecessary computational process and/or calculations and local extrema (due to the high fluctuation behaviors at the maximum magnitude of the spurious velocity). When the maximum spurious velocity becomes on the order of 10^{-6} for more than ten times constantly, the system is assumed to be at the equilibrium state. The animations of density and pressure variations during different time steps can visualize and identify this specific condition. It should be noted that the simulation run (referring to Fig. 5) is not performed at the same condition that Yuan and Schaefer conducted their modeling (simulation) work [55]. However, the same order of magnitude for the maximum spurious velocity in the case of PR EOS was reported by Yuan and Schaefer.

III. LIMITATIONS

The proposed single-relaxation time collision (BGK) is appropriate for low Reynolds number (particularly stationary) cases. To extend the model to high Reynolds number conditions, the multirelaxation time (MRT) collision scheme is proposed [73,74].

In the CPA EOS, it is assumed that the activity of each bonding site is independent of other bonding sites in the molecule, implying negligence of the steric hindrance and cooperativity effects. The polarity and quadrupolar interactions are also disregarded in the proposed model [75,76].

IV. RESULTS AND DISCUSSION

In this section, the consistency of the CPA EOS case is examined. Simulation outputs of the CPA and PR EOSs are presented and then a comparison between the modeling results and real saturation data is made. The Li *et al.* forcing scheme is employed to achieve an improvement in thermodynamic consistency and spurious velocity distribution. The discrete gradient operator with a higher isotropic order is used to

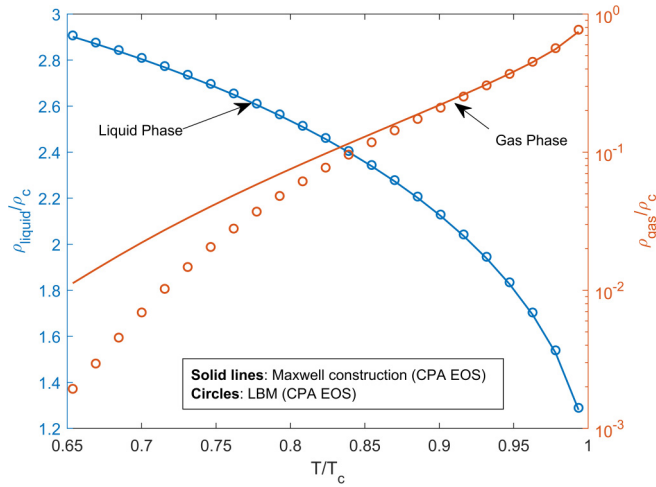


FIG. 6. Comparison of coexistence curves based on LBM simulations and Maxwell construction.

lower the spurious velocity, while the modified CPA EOS is implemented to determine the initial density.

The effectiveness and/or reliability of the proposed model are assessed by comparison of the LBM simulation results with the outputs of the Maxwell construction approach. Figure 6 illustrates the coexistence of density and/or reduced temperature curves attained from the Maxwell construction and the LBM simulations when utilizing the CPA EOS. As it is clear from Fig. 6, an acceptable match is achieved for the liquid branch; however, the difference between the LBM and Maxwell construction results is noticeable for the gas phase.

To explain this considerable deviation, the gas branch is simulated based on both CPA and PR EOSs as shown in Fig. 7 in the semi-log-scale where the LBM and Maxwell construction strategies are employed. According to Fig. 7, the difference between the PR-LBM and CPA-LBM cases will increase as the temperature decreases. As expected,

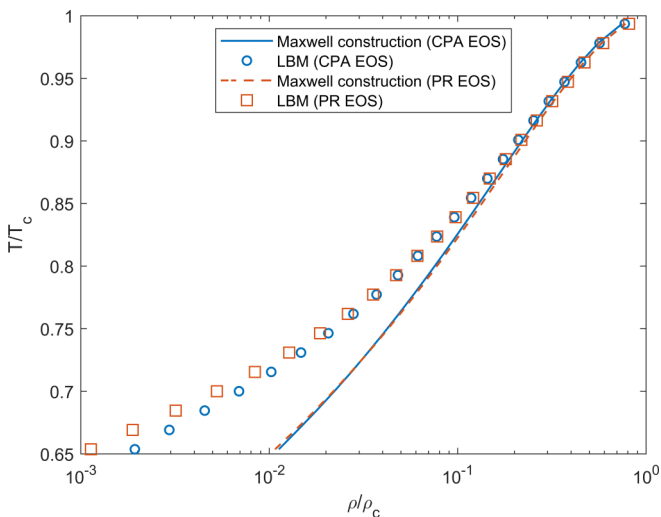


FIG. 7. Comparison between the reduced densities of the gas phase of the coexistence phases determined from the LBM simulation and Maxwell construction when PR and CPA EOSs are employed.

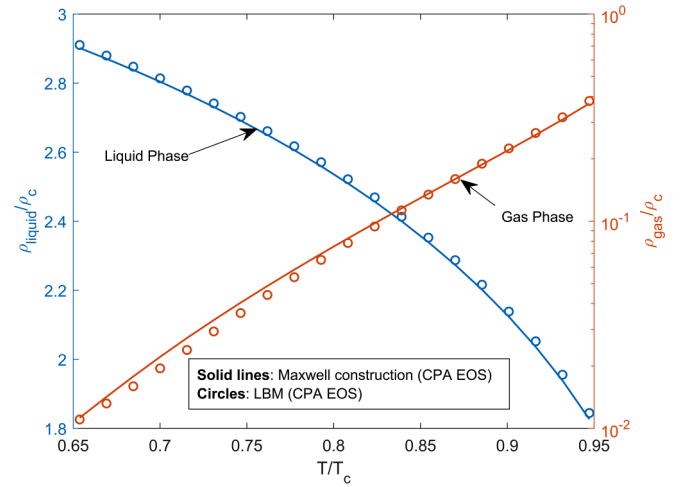


FIG. 8. Reduced density of both liquid and gas phases versus reduced temperature based on LBM simulations and Maxwell construction when the Li *et al.* forcing scheme is employed.

such a deviation is not observed for the PR and CPA EOSs while using the Maxwell construction. The relative errors ($|\rho_{LBM} - \rho_{Mc}|/\rho_{Mc}$), where ρ_{LBM} and ρ_{Mc} are the gas density calculated from the LBM simulation and Maxwell construction, are 3.3612% and 4.4223% at $T_r = 0.65$ for the gas phase modeled by the CPA and PR EOSs, respectively. The difference between the mechanical stable results (e.g., LBM results) and thermodynamically stable results (e.g., Maxwell results) for the gas phase is due to the curved interface of the droplet and/or additional term which is introduced into the macroscopic equations when the velocity-shift (or Shan-Chen) forcing scheme is used. Li *et al.* showed that ϵ in Eq. (12) should be between $\epsilon = 1$ and $\epsilon = 2$ to obtain a better agreement with the Maxwell construction [1].

Thus, the thermodynamic inconsistency is tackled through different approaches such as multipseudopotential interaction [52,53] and improved force scheme in multirelaxation time LBM to enhance the model reliability [73,77]. The self-tuning EOS is also employed to achieve more stable results [71,78].

Through implementation of the Li *et al.* forcing scheme, it is expected to improve the thermodynamic consistency. Figure 8 illustrates the thermodynamic consistency of the LBM method when CPA EOS is utilized with $\sigma' = 0.2885$ [see Eq. (13)]. As seen in Fig. 8, there is a very good match between the LBM and Maxwell construction outputs. In addition, the thermodynamic consistency in the gas phase is improved considerably. However, a small deviation in the liquid phase is noticed. The association parameters of CPA EOS (e.g., $\epsilon^{A_i K_i}$ and $\beta^{A_i K_i}$) are selected to attain a good match with the experimental data while employing the velocity-shifting forcing scheme. Therefore, the thermodynamic consistency in the liquid phase might decrease slightly when the magnitude of σ' is increased to improve the thermodynamic consistency in the gas phase. To overcome this problem, the parameter σ' is used in the Li *et al.* forcing scheme to modify the interaction properties. Li *et al.* proved that the model will be unstable when $\sigma' = 0$ (e.g., the Guo *et al.* forcing scheme), due to the high thermodynamic inconsistency.

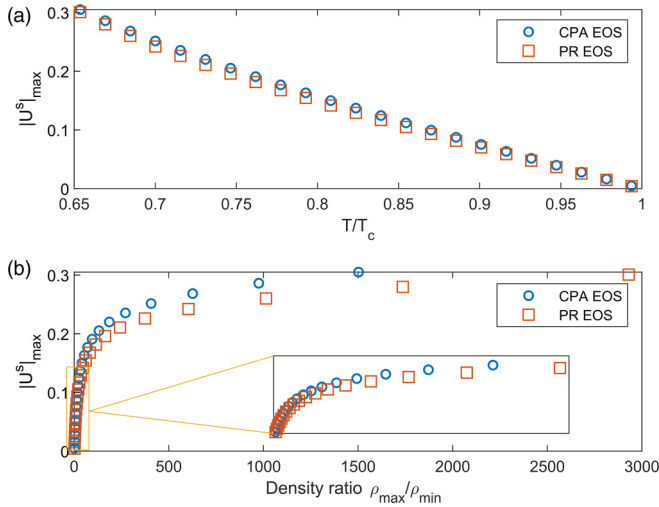


FIG. 9. Variation of the maximum magnitude of spurious velocity with (a) reduced temperature and (b) density ratio for the CPA and PR EOSs.

The numerical stability of the integrated CPA-LBM model can be evaluated based on the maximum magnitude of the spurious velocity, $|u^s|_{\max}$. Figure 9 compares the $|u^s|_{\max}$ trends for both CPA-LBM and PR-LBM cases at different reduced temperatures [panel (a) of Fig. 9] and density ratios [panel (b) of Fig. 9]. According to Fig. 9, the value of the spurious velocity is increased with decreasing the reduced temperature for both CPA and PR EOSs. The lower density ratio does not reveal the lower capability of the CPA-LBM approach that might be due to the higher density in the gas phase (see Fig. 7). The maximum magnitude of spurious velocity is not changed considerably when the implemented EOS is switched from PR to CPA, since the extent of spurious velocity is mainly affected by the order of isotropy in the gradient operator and the forcing scheme.

The differences between the magnitudes of spurious velocity obtained in the current study (see Fig. 9) and previous studies might be due to the simulation inputs and stability condition. Providing more information, Yuan and Schaefer’s simulations were conducted at a $50 \times 50 \times 50$ lattice domain with an initial liquid droplet size of $r_{\text{init}} = 10$ [55]. Also, the stability condition in their study is assumed as 30000 time steps for the initial run as well as for checking the stability

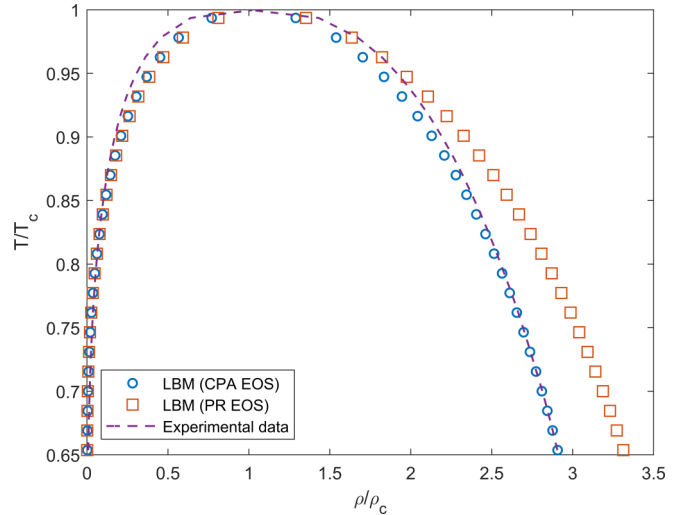


FIG. 11. Comparison of the values of saturated water density obtained from experiments and LBM strategy based on CPA and PR EOSs.

condition for each of 1000 time steps. Their steady-state condition should be met once, which is not appropriate for such a fluctuating behavior.

It should be noted that the results shown in Fig. 9 are based on the SC forcing scheme (known as the velocity shift method). To elaborate the impact of the forcing scheme, the contour map and velocity field of a static droplet are depicted in Fig. 10 for both Li *et al.* and SC forcing schemes when $T/T_c = 0.9$ and $\tau = 1$.

As shown in Fig. 10, the Li *et al.* forcing scheme exhibits lower spurious velocities. Based on the velocity contour profile, the velocity distribution patterns are also different for these two different forcing schemes, implying that the Li *et al.* forcing scheme is able to better demonstrate the flow behaviors obtained from the Navier-Stokes equations, compared to the SC forcing scheme. Hence, it appears to be a better representation of the isotropy in the LBM discrete gradient operator.

To examine the capability of the CPA-LBM strategy to model the real data, a comparison between the experimental data of water and simulation results is made. Figure 11 presents the results of the CPA-LBM simulations

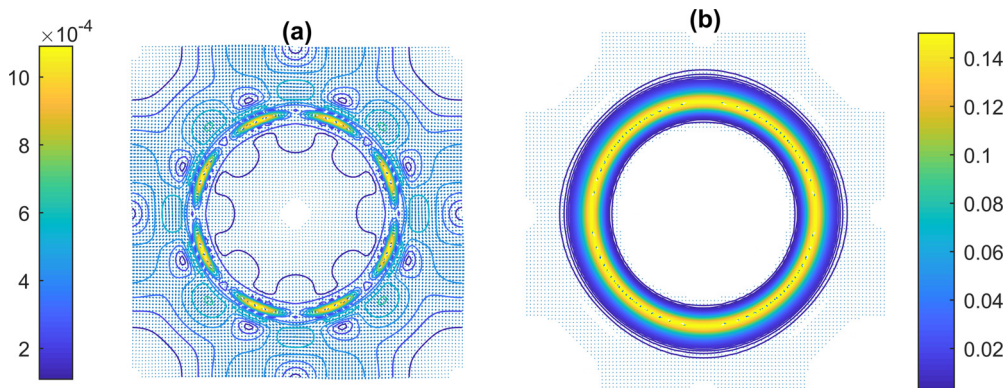


FIG. 10. Velocity field and contour for a static droplet on the basis of (a) Li *et al.* and (b) SC forcing schemes.

TABLE I. Error comparison of CPA and PR results obtained from LBM simulation.

EOS	Max error (%)	Min error (%)	Mean-squared error
CPA	76.0435	0.0169	0.0030
PR	87.8518	0.0546	0.0355

for estimation of the liquid phase density, where the SC forcing scheme is employed. As illustrated in Fig. 11, the CPA EOS offers a greater precision for both phases, compared to the PR EOS case. Table I presents a comparison of the results obtained from both CPA and PR EOSs. According to Table I, CPA has a lower error percentage (e.g., minimum error, maximum error, and mean-squared error), compared to PR. As the parameters for the association part of the CPA EOS (e.g., ϵ and β) approach zero, the results of the CPA EOS become closer to the PR EOS simulation outputs. Therefore, it is vital to determine the associating parameters in the lattice units with a high accuracy to attain reliable trends and/or outcome. As explained in Methodology, the association parameters for water in the lattice units are $\epsilon = 0.1636$ and $\beta = 0.0973$. Table II summarizes the self-association energy and bonding volume parameters for five associating fluids including water, methanol, ethanol, 1-propanol, and 1-butanol. It is worth noting that the global search optimization is chosen to avoid the local optima, although the initial guesses might still affect the final optimal points.

Li *et al.* concluded that a lower value for the attraction parameter (a) in EOS results in a greater stability at lower reduced temperatures [73]. Therefore, the CPA EOS association parameters are listed in Table III for lower values of the attraction parameter. As mentioned earlier, the 4C and 2B bonding schemes are employed for water and alcohols, respectively.

Up to now, all LBM results have been obtained based on the fourth-order isotropy of the discrete gradient operator. As it is known, increasing the isotropy order leads to a decrease in the spurious velocity [49,50]. Our plan is to investigate the impact of isotropic order of the discrete gradient operator up to eighth order on the simulation outputs. It was found that the system becomes unstable due to low interfacial tension at low reduced temperature and/or high density ratio conditions. Therefore, an extended version of the CPA EOS is used to determine the initial density distribution.

TABLE II. Associating parameters in the lattice units suggested for water and normal alcohols (from methanol to 1-butanol) while implementing the global search optimization ($a = 2/49$, $b = 2/21$, and $R = 1$).

Compound	ω	ϵ^{AB}	β	R_{squared}
Water	0.344	0.1636	0.09730	0.9992
Methanol	0.565	0.5638	0.0733	0.9984
Ethanol	0.643	0.6086	0.0727	0.9979
1-Propanol	0.620	0.5324	0.0877	0.9984
1-Butanol	0.588	0.5994	0.0828	0.9988

TABLE III. Associating parameters in the lattice units for pure compounds such as water and normal alcohols (from methanol to 1-butanol) using the global search optimization when $b = 2/21$ and $R = 1$.

Compound	$a = 1/49$			$a = 1/98$		
	ϵ^{AB}	β	R_{squared}	ϵ^{AB}	β	R_{squared}
Water	0.0819	0.0972	0.9992	0.0433	0.0854	0.9992
Methanol	0.3795	0.0505	0.9983	0.2526	0.0372	0.9983
Ethanol	0.3730	0.0569	0.9979	0.2561	0.0401	0.9979
1-Propanol	0.3966	0.0538	0.9983	0.2498	0.0419	0.9983
1-Butanol	0.4247	0.0537	0.9987	0.2522	0.0451	0.9987

Figure 12 presents the LBM results using eighth order of isotropy. To obtain the initial density distribution function, (80, 0.5) is selected as the pair of input parameters of the extended CPA EOS. The Li *et al.* forcing scheme is applied to improve the thermodynamic consistency. Considering the same input parameter of the extended model for the entire temperature interval can cause high computational costs. Additionally, assuming the same σ' as an input parameter for the reduced temperature leads to an appreciable departure from the Maxwell equal area construction (see Fig. 12). Hence, a smart method can be utilized to choose a suitable pair input parameter for the extended CPA EOS, (α , κ), and the input parameter of Li *et al.*'s forcing scheme at each temperature. Such a strategy can decrease the computational costs and improve the thermodynamic consistency.

To study the capillary effect, the simulation runs need to be conducted at different droplet radii. The slope of differential pressure between the gas and liquid phases (e.g., capillary pressure) versus the inverse of the radius is then related to the interfacial tension [see Eq. (A6)]. Figure 13 illustrates the variations of the capillary pressure with the inverse of the droplet radius for water at $T_r = 0.7929$. In other words,

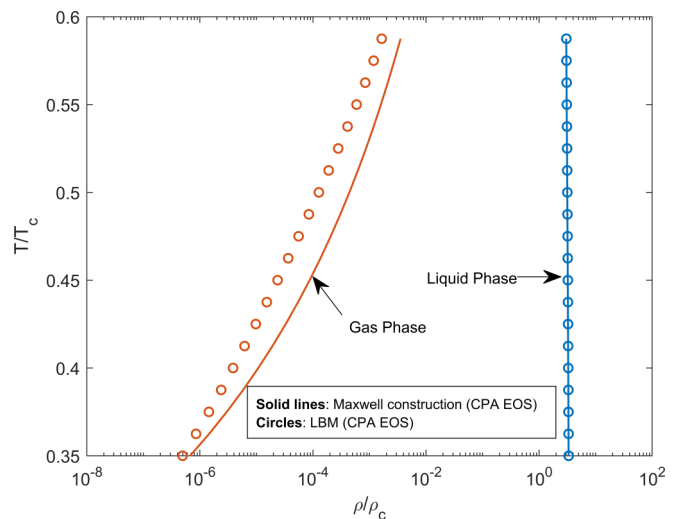


FIG. 12. Coexistence curves results of the LBM simulation and Maxwell equal area construction with eighth order of isotropy in the discrete gradient operator.

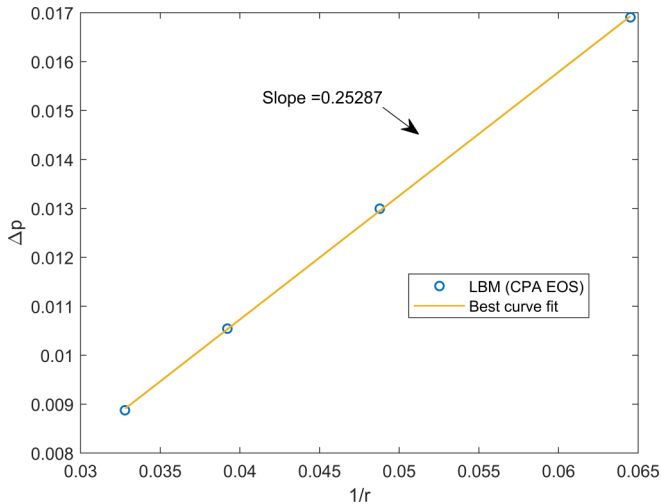


FIG. 13. The pressure difference (Δp) against $1/r$ for water at $T_r = 0.7929$.

the applicability of the Laplace law, which expresses a linear relationship between the droplet radius and pressure difference, is demonstrated in Fig. 13. In spite of the multirange pseudopotential approach [2–4], the interfacial tension is a function of the fluid type in this study where the single-range pseudopotential method is utilized. The interfacial tension can be tuned by including the multirange potential in the improved forcing term of MRT LBM [79,80]. The influence of droplet size can be minimized by the use of self-tuning equation of state [71]. Li and Luo concluded that the droplet size impact on the gas-phase density can be reduced by increasing the slope of EOS in the vapor phase [78].

The same procedure is followed at different reduced temperatures to figure out the trend and/or behaviors of the interfacial tension, σ , with temperature. The interfacial tension of water versus reduced temperature is shown in Fig. 14. As it is clear, the interfacial tension results attained from LBM simulations follow the same trend and/or behaviors

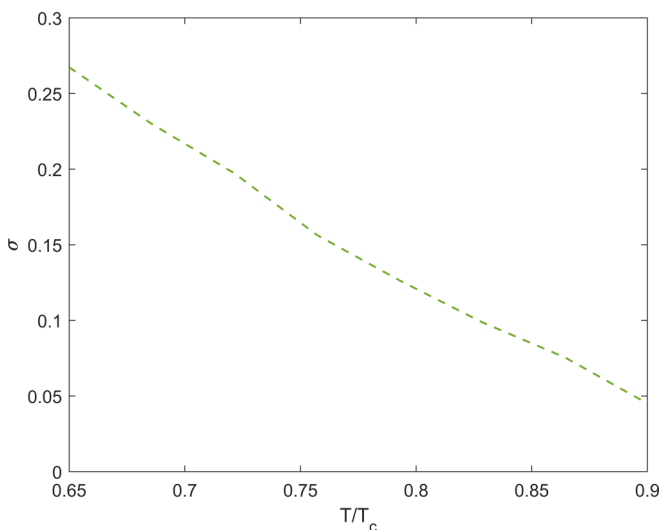


FIG. 14. Interfacial tension versus the reduced temperature in the lattice units for water.

as the measured values (real data). Due to implementation of the single-range pseudopotential approach in the current study, the interfacial tension cannot be tuned. To address this limitation, the multirange pseudopotential is introduced [81–83].

Associating fluids play a crucial role in different processes and/or phenomena such as biological processes [84], oil production (recovery) from hydrocarbon reservoirs [20], energy systems, and chemical production. Therefore, development of a reliable LBM approach to simulate the thermodynamic characteristics of associating fluids seems vital to better design and operate the corresponding processes. The methodology proposed in this research work is appropriate for static problems by using the BGK collision scheme. The MRT collision scheme can be an appropriate alternative to extend this approach to the cases at high Reynolds number conditions. Also, the cascaded model can be used to improve the ability of the LBM for fluid flow and thermal transport modeling. The cascaded model, which is also known as the central-moment-based lattice Boltzmann method, is proposed to tackle the numerical instability in the zero-viscosity limit. This generally happens by an insufficient degree of Galilean invariance of the relaxation-type lattice Boltzmann collision operation [85].

V. CONCLUSIONS

Some fluids associate due to the hydrogen bonding. This association results in unusual thermodynamic behaviors. In this research work, the CPA EOS is included in the LBM to model the thermodynamic behaviors of this type of fluids. The method accuracy is verified with the Maxwell construction approach and experimental data. The main conclusions drawn based on the study results are listed below:

(i) A more reliable stability condition is proposed to decrease the computational costs. Furthermore, a better thermodynamic consistency in the gas phase is attained by implementing the CPA EOS in the LBM.

(ii) An approach based on the global search optimization method is developed to determine the association parameters in the lattice units for water and primary alcohols (e.g., methanol and 1-butanol).

(iii) There is a very good agreement between the CPA-LBM results and experimental data, while the PR-LBM case is not able to simulate the real thermodynamic behaviors with an acceptable accuracy.

(iv) The thermodynamic consistency is enhanced by employing the Li *et al.* forcing scheme. It is also possible to maintain the stability and thermodynamic consistency at low reduced temperatures through using higher orders of isotropy in the gradient operator.

(v) An extended version of CPA EOS is introduced to determine the initial density distribution, making the computation faster and more reliable.

(vi) The interfacial tension of water as a function of the reduced temperature is acceptably simulated with the CPA-LBM approach.

(vii) In the current study, the single-range approach is implemented. In the single-range approach, only one strength parameter is used which is canceled out when an EOS is

employed. The multirange pseudopotential can handle the interfacial tension and improve the stability. Modification and utilization of the multirange pseudopotential approach is the scope of our future work.

ACKNOWLEDGMENTS

The authors wish to acknowledge the support of Memorial University, Canada; the Natural Sciences and Engineering Research Council of Canada (NSERC); InnovateNL; and Equinor (formerly Statoil) Canada.

APPENDIX: MAXWELL CONSTRUCTION AND COMPUTATION ALGORITHM

The equality of the Gibbs free energy at the saturation point for a droplet is expressed as follows:

$$G^l = G^g, \tag{A1}$$

$$A^l + P^l v^l = A^g + P^g v^g, \tag{A2}$$

where G and A represent the Gibbs and Helmholtz free energies, respectively. For flat interfaces, both pressures in the liquid and gas phases are equal to the saturation pressure, as shown below:

$$P^l = P^g = P^{\text{sat}}, \tag{A3}$$

Since $dT = 0$ (isothermal condition) at the equilibrium, we can write the following equation:

$$A^g - A^l = - \int P dv. \tag{A4}$$

Using Eqs. (A2) to (A4), the saturation coexistence densities can be calculated through using the following equation:

$$- \int_{v_l}^{v_g} P dv = -P^{\text{sat}}(v^l - v^g). \tag{A5}$$

To calculate the coexistence volumes (densities), first an initial saturation pressure is guessed. Based on the initial guess, the liquid and gas volumes (densities) are calculated using an EOS. If the left-hand side (LHS) is more than the right-hand side (RHS), the pressure for the next loop should be increased to obtain the correct value; otherwise, it should be decreased. This loop will be repeated until the relative differences between two loops are very small (10^{-10}).

The guessed initial pressure should be between the spinodal points where $dP/dv = 0$. Due to the nonlinearity of the CPA EOS, the first spinodal point (e.g., with a lower volume) is determined by finding the global minimum of CPA EOS.

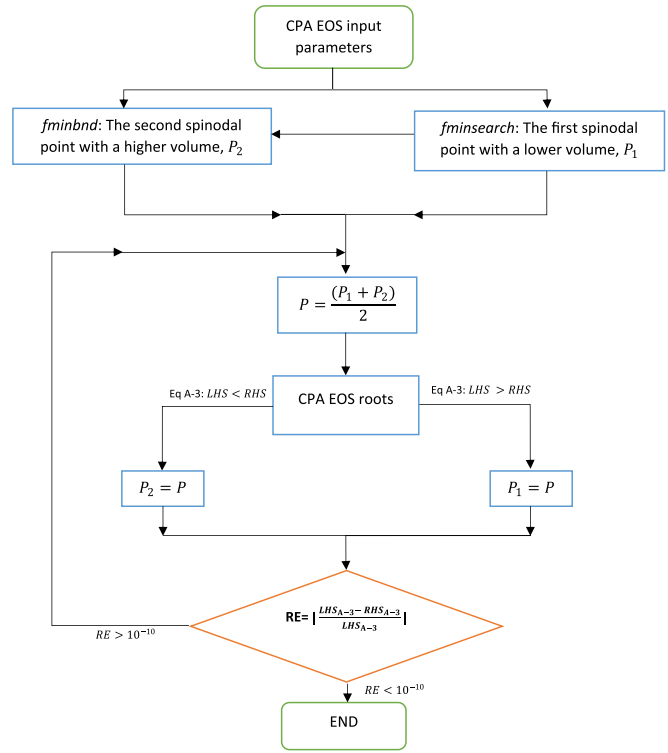


FIG. 15. Workflow of Maxwell construction while utilizing CPA EOS (RE stands for the relative error).

Searching the global minimum is started from the repulsion parameter [e.g., b in Eq. (14)]. The second spinodal point, which has a higher volume than the first spinodal point, is then determined through finding the global maximum point. Searching the global maximum is also commenced from the first spinodal point. The *fminsearch* and *fminbnd* MATLAB functions are utilized to determine the minimum and maximum spinodal points, respectively. To obtain the roots of CPA EOS, a MATLAB intrinsic solver (e.g., *fsolve*) is employed [69]. The initial guesses for the CPA EOS roots are chosen based on the roots of the PR EOS. The procedure on the Maxwell construction is demonstrated in Fig. 15.

When the interface between two phases is curved, the Young-Laplace equation of capillarity provides the mechanical equilibrium for a droplet, as given below [86]:

$$P^l - P^g = P_c = \frac{2\sigma}{r}, \tag{A6}$$

in which P_c is the capillary pressure; P^l is the liquid pressure; P^g introduces the gas pressure; σ refers to the interfacial tension; and r stands for the radius of the droplet.

[1] Q. Li, K. H. Luo, Q. Kang, Y. He, Q. Chen, and Q. Liu, Lattice Boltzmann methods for multiphase flow and phase-change heat transfer, *Prog. Energy Combust. Sci.* **52**, 62 (2016).
 [2] J.-M. Vanson, F. o.-X. Coudert, M. Klotz, and A. Boutin, Kinetic accessibility of porous material adsorption sites studied through the lattice Boltzmann method, *Langmuir* **33**, 1405 (2017).

[3] D.-Y. Peng and D. B. Robinson, A new two-constant equation of state, *Ind. Eng. Chem. Fundam.* **15**, 59 (1976).
 [4] G. Soave, Equilibrium constants from a modified Redlich-Kwong equation of state, *Chem. Eng. Sci.* **27**, 1197 (1972).
 [5] G. M. Kontogeorgis, M. L. Michelsen, G. K. Folas, S. Derawi, N. von Solms, and E. H. Stenby, Ten years with the CPA (Cubic-Plus-Association) equation of state. Part 1. Pure

- compounds and self-associating systems, *Ind. Eng. Chem. Res.* **45**, 4855 (2006).
- [6] A. Firoozabadi, *Thermodynamics and Applications in Hydrocarbon Energy Production* (McGraw-Hill Education, New York, 2016).
- [7] G. M. Kontogeorgis, E. C. Voutsas, I. V. Yakoumis, and D. P. Tassios, An equation of state for associating fluids, *Ind. Eng. Chem. Res.* **35**, 4310 (1996).
- [8] Z. Li and A. Firoozabadi, Cubic-plus-association equation of state for water-containing mixtures: Is “cross association” necessary? *AIChE J.* **55**, 1803 (2009).
- [9] Z. Li and A. Firoozabadi, Cubic-plus-association equation of state for asphaltene precipitation in live oils, *Energy Fuels* **24**, 2956 (2010).
- [10] Z. Li and A. Firoozabadi, Modeling asphaltene precipitation by n-alkanes from heavy oils and bitumens using cubic-plus-association equation of state, *Energy Fuels* **24**, 1106 (2010).
- [11] G. M. Kontogeorgis, M. L. Michelsen, G. K. Folas, S. Derawi, N. von Solms, and E. H. Stenby, Ten years with the CPA (Cubic-Plus-Association) equation of state. Part 2. Cross-associating and multicomponent systems, *Ind. Eng. Chem. Res.* **45**, 4869 (2006).
- [12] G. R. McNamara and G. Zanetti, Use of the Boltzmann Equation to Simulate Lattice-Gas Automata, *Phys. Rev. Lett.* **61**, 2332 (1988).
- [13] U. Frisch, B. Hasslacher, and Y. Pomeau, Lattice-Gas Automata for the Navier-Stokes Equation, *Phys. Rev. Lett.* **56**, 1505 (1986).
- [14] S. Chen and G. D. Doolen, Lattice Boltzmann method for fluid flows, *Ann. Rev. Fluid Mech.* **30**, 329 (1998).
- [15] N. Gupta, E. Fathi, and F. Belyadi, Effects of nano-pore wall confinements on rarefied gas dynamics in organic rich shale reservoirs, *Fuel* **220**, 120 (2018).
- [16] S. Tao and Z. Guo, Boundary condition for lattice Boltzmann modeling of microscale gas flows with curved walls in the slip regime, *Phys. Rev. E* **91**, 043305 (2015).
- [17] L. Yang, Y. Yu, G. Hou, K. Wang, and Y. Xiong, Boundary conditions with adjustable slip length for the lattice Boltzmann simulation of liquid flow, *Comput. Fluids* **174**, 200 (2018).
- [18] R. H. H. Abadi, A. Fakhari, and M. H. Rahimian, Numerical simulation of three-component multiphase flows at high density and viscosity ratios using lattice Boltzmann methods, *Phys. Rev. E* **97**, 033312 (2018).
- [19] L. Chen, Q. Kang, Y. Mu, Y.-L. He, and W.-Q. Tao, A critical review of the pseudopotential multiphase lattice Boltzmann model: Methods and applications, *Int. J. Heat Mass Transfer* **76**, 210 (2014).
- [20] H. Liu, Q. Kang, C. R. Leonardi, S. Schmieschek, A. Narváez, B. D. Jones, J. R. Williams, A. J. Valocchi, and J. Harting, Multiphase lattice Boltzmann simulations for porous media applications, *Comput. Geosci.* **20**, 777 (2016).
- [21] Y.-L. He, Q. Liu, Q. Li, and W.-Q. Tao, Lattice Boltzmann methods for single-phase and solid-liquid phase-change heat transfer in porous media: A review, *Int. J. Heat Mass Transfer* **129**, 160 (2019).
- [22] R. Arabjamaloei and D. Ruth, Numerical study of inertial effects on permeability of porous media utilizing the Lattice Boltzmann Method, *J. Nat. Gas Sci. Eng.* **44**, 22 (2017).
- [23] Z. Chai, B. Shi, J. Lu, and Z. Guo, Non-Darcy flow in disordered porous media: A lattice Boltzmann study, *Comput. Fluids* **39**, 2069 (2010).
- [24] S. Foroughi, S. Jamshidi, and M. R. Pishvaie, New correlative models to improve prediction of fracture permeability and inertial resistance coefficient, *Transp. Porous Media* **121**, 557 (2018).
- [25] M. Hasert, J. Bernsdorf, and S. Roller, Lattice Boltzmann simulation of non-Darcy flow in porous media, *Procedia CS* **4**, 1048 (2011).
- [26] M. C. Sukop, H. Huang, P. F. Alvarez, E. A. Variano, and K. J. Cunningham, Evaluation of permeability and non-Darcy flow in vuggy macroporous limestone aquifer samples with lattice Boltzmann methods, *Water Resour. Res.* **49**, 216 (2013).
- [27] Z. Chai, N. He, Z. Guo, and B. Shi, Lattice Boltzmann model for high-order nonlinear partial differential equations, *Phys. Rev. E* **97**, 013304 (2018).
- [28] H. Lai and C. Ma, A higher order lattice BGK model for simulating some nonlinear partial differential equations, *Sci. China Ser. G: Phys. Mech. Astron.* **52**, 1053 (2009).
- [29] B. Shi and Z. Guo, Lattice Boltzmann model for nonlinear convection-diffusion equations, *Phys. Rev. E* **79**, 016701 (2009).
- [30] B. Shi and Z. Guo, Lattice Boltzmann simulation of some nonlinear convection-diffusion equations, *Comput. Math. Appl.* **61**, 3443 (2011).
- [31] H. Wang, B. Shi, H. Liang, and Z. Chai, Finite-difference lattice Boltzmann model for nonlinear convection-diffusion equations, *Appl. Math. Comput.* **309**, 334 (2017).
- [32] L. Zhang, S. Yang, Z. Zeng, and J. W. Chew, Consistent boundary conditions of the multiple-relaxation-time lattice Boltzmann method for convection-diffusion equations, *Comput. Fluids* **170**, 24 (2018).
- [33] T. Krüger, S. Frijters, F. Günther, B. Kaoui, and J. Harting, Numerical simulations of complex fluid-fluid interface dynamics, *Eur. Phys. J.: Spec. Top.* **222**, 177 (2013).
- [34] G. Tryggvason, B. Bunner, A. Esmaeeli, D. Juric, N. Al-Rawahi, W. Tauber, J. Han, S. Nas, and Y.-J. Jan, A front-tracking method for the computations of multiphase flow, *J. Comput. Phys.* **169**, 708 (2001).
- [35] J. A. Sethian and P. Smereka, Level set methods for fluid interfaces, *Ann. Rev. Fluid Mech.* **35**, 341 (2003).
- [36] C. W. Hirt and B. D. Nichols, Volume of fluid (VOF) method for the dynamics of free boundaries, *J. Comput. Phys.* **39**, 201 (1981).
- [37] V. Badalassi, H. Cenicerros, and S. Banerjee, Computation of multiphase systems with phase field models, *J. Comput. Phys.* **190**, 371 (2003).
- [38] A. K. Gunstensen, D. H. Rothman, S. Zaleski, and G. Zanetti, Lattice Boltzmann model of immiscible fluids, *Phys. Rev. A* **43**, 4320 (1991).
- [39] D. H. Rothman and J. M. Keller, Immiscible cellular-automaton fluids, *J. Stat. Phys.* **52**, 1119 (1988).
- [40] M. R. Swift, W. Osborn, and J. Yeomans, Lattice Boltzmann Simulation of Nonideal Fluids, *Phys. Rev. Lett.* **75**, 830 (1995).
- [41] X. He, S. Chen, and R. Zhang, A lattice Boltzmann scheme for incompressible multiphase flow and its application in simulation of Rayleigh-Taylor instability, *J. Comput. Phys.* **152**, 642 (1999).

- [42] X. Shan and H. Chen, Lattice Boltzmann model for simulating flows with multiple phases and components, *Phys. Rev. E* **47**, 1815 (1993).
- [43] R. Benzi, S. Succi, and M. Vergassola, The lattice Boltzmann equation: Theory and applications, *Phys. Rep.* **222**, 145 (1992).
- [44] H. Huang, M. Sukop, and X. Lu, *Multiphase Lattice Boltzmann Methods: Theory and Application* (John Wiley & Sons, Chichester, UK, 2015).
- [45] S. Succi, *The Lattice Boltzmann Equation: For Fluid Dynamics and Beyond* (Clarendon, Oxford, 2001).
- [46] S. Succi, *The Lattice Boltzmann Equation: For Complex States of Flowing Matter* (Oxford University Press, Oxford, 2018).
- [47] D. A. Wolf-Gladrow, *Lattice-gas Cellular Automata and Lattice Boltzmann Models: An Introduction* (Springer, New York, 2004).
- [48] M. R. Parsa and A. J. Wagner, Lattice gas with molecular dynamics collision operator, *Phys. Rev. E* **96**, 013314 (2017).
- [49] X. Shan, Analysis and reduction of the spurious current in a class of multiphase lattice Boltzmann models, *Phys. Rev. E* **73**, 047701 (2006).
- [50] M. Sbragaglia, R. Benzi, L. Biferale, S. Succi, K. Sugiyama, and F. Toschi, Generalized lattice Boltzmann method with multirange pseudopotential, *Phys. Rev. E* **75**, 026702 (2007).
- [51] M. Sbragaglia and X. Shan, Consistent pseudopotential interactions in lattice Boltzmann models, *Phys. Rev. E* **84**, 036703 (2011).
- [52] S. Khajepor, J. Wen, and B. Chen, Multipseudopotential interaction: A solution for thermodynamic inconsistency in pseudopotential lattice Boltzmann models, *Phys. Rev. E* **91**, 023301 (2015).
- [53] S. Khajepor and B. Chen, Multipseudopotential interaction: A consistent study of cubic equations of state in lattice Boltzmann models, *Phys. Rev. E* **93**, 013303 (2016).
- [54] Q. Li, K. H. Luo, and X. J. Li, Forcing scheme in pseudopotential lattice Boltzmann model for multiphase flows, *Phys. Rev. E* **86**, 016709 (2012).
- [55] P. Yuan and L. Schaefer, Equations of state in a lattice Boltzmann model, *Phys. Fluids* **18**, 042101 (2006).
- [56] A. Kupershtokh, D. Medvedev, and D. Karpov, On equations of state in a lattice Boltzmann method, *Comput. Math. Appl.* **58**, 965 (2009).
- [57] J. Zhang and F. Tian, A bottom-up approach to non-ideal fluids in the lattice Boltzmann method, *EPL* **81**, 66005 (2008).
- [58] M. Sukop and D. Thorne, *Lattice Boltzmann Modeling: An Introduction for Geoscientists and Engineers* (Springer-Verlag, Berlin, 2006).
- [59] P. L. Bhatnagar, E. P. Gross, and M. Krook, A model for collision processes in gases. I. small amplitude processes in charged and neutral one-component systems, *Phys. Rev.* **94**, 511 (1954).
- [60] X. Shan, X.-F. Yuan, and H. Chen, Kinetic theory representation of hydrodynamics: A way beyond the Navier–Stokes equation, *J. Fluid Mech.* **550**, 413 (2006).
- [61] X. Shan, Pressure tensor calculation in a class of nonideal gas lattice Boltzmann models, *Phys. Rev. E* **77**, 066702 (2008).
- [62] R. Benzi, L. Biferale, M. Sbragaglia, S. Succi, and F. Toschi, Mesoscopic modeling of a two-phase flow in the presence of boundaries: The contact angle, *Phys. Rev. E* **74**, 021509 (2006).
- [63] Z. Guo, C. Zheng, and B. Shi, Discrete lattice effects on the forcing term in the lattice Boltzmann method, *Phys. Rev. E* **65**, 046308 (2002).
- [64] W. G. Chapman, K. E. Gubbins, G. Jackson, and M. Radosz, New reference equation of state for associating liquids, *Ind. Eng. Chem. Res.* **29**, 1709 (1990).
- [65] M. L. Michelsen and E. M. Hendriks, Physical properties from association models, *Fluid Phase Equilib.* **180**, 165 (2001).
- [66] E. Hendriks, J. Walsh, and A. Van Bergen, A general approach to association using cluster partition functions, *J. Stat. Phys.* **87**, 1287 (1997).
- [67] S. H. Huang and M. Radosz, Equation of state for small, large, polydisperse, and associating molecules, *Ind. Eng. Chem. Res.* **29**, 2284 (1990).
- [68] Toronto maple: Maplesoft, a division of Waterloo Maple Inc. (2017).
- [69] MATLAB, The MathWorks, Inc., Natick, Massachusetts, R2018b.
- [70] Z. Ugray, L. Lasdon, J. Plummer, F. Glover, J. Kelly, and R. Martí, Scatter search and local NLP solvers: A multistart framework for global optimization, *INFORMS J. Comput.* **19**, 328 (2007).
- [71] C. E. Colosqui, G. Falcucci, S. Ubertini, and S. Succi, Mesoscopic simulation of non-ideal fluids with self-tuning of the equation of state, *Soft Matter* **8**, 3798 (2012).
- [72] H. Huang, M. Krafczyk, and X. Lu, Forcing term in single-phase and Shan-Chen-type multiphase lattice Boltzmann models, *Phys. Rev. E* **84**, 046710 (2011).
- [73] Q. Li, K. Luo, and X. Li, Lattice Boltzmann modeling of multiphase flows at large density ratio with an improved pseudopotential model, *Phys. Rev. E* **87**, 053301 (2013).
- [74] Z. Yu and L.-S. Fan, Multirelaxation-time interaction-potential-based lattice Boltzmann model for two-phase flow, *Phys. Rev. E* **82**, 046708 (2010).
- [75] M. G. Bjørner and G. M. Kontogeorgis, Modeling derivative properties and binary mixtures with CO₂ using the CPA and the quadrupolar CPA equations of state, *Fluid Phase Equilib.* **408**, 151 (2016).
- [76] M. G. Bjørner, G. Sin, and G. M. Kontogeorgis, Uncertainty analysis of the CPA and a quadrupolar CPA equation of state—With emphasis on CO₂, *Fluid Phase Equilib.* **414**, 29 (2016).
- [77] L. Zhang, T. Ku, J. Jia, and X. Cheng, The role of wettability of nonideal nozzle plate: From drop-on-demand droplet jetting to impact on solid substrate, *AIChE J.* **64**, 2837 (2018).
- [78] Q. Li and K. Luo, Thermodynamic consistency of the pseudopotential lattice Boltzmann model for simulating liquid–vapor flows, *Appl. Therm. Eng.* **72**, 56 (2014).
- [79] Q. Li and K. Luo, Achieving tunable surface tension in the pseudopotential lattice Boltzmann modeling of multiphase flows, *Phys. Rev. E* **88**, 053307 (2013).
- [80] A. Xu, T. Zhao, L. An, and L. Shi, A three-dimensional pseudopotential-based lattice Boltzmann model for multiphase flows with large density ratio and variable surface tension, *Int. J. Heat Fluid Flow* **56**, 261 (2015).
- [81] G. Falcucci, G. Bella, G. Chiatti, S. Chibbaro, M. Sbragaglia, and S. Succi, Lattice Boltzmann models with mid-range interactions, *Commun. Comput. Phys.* **2**, 1071 (2007).
- [82] G. Falcucci, S. Ubertini, C. Biscarini, S. Di Francesco, D. Chiappini, S. Palpacelli, A. De Maio, and S. Succi, Lattice Boltzmann methods for multiphase flow simulations across scales, *Commun. Comput. Phys.* **9**, 269 (2011).

- [83] G. Falcucci, S. Ubertini, and S. Succi, Lattice Boltzmann simulations of phase-separating flows at large density ratios: The case of doubly-attractive pseudo-potentials, *Soft Matter* **6**, 4357 (2010).
- [84] A. Montessori, I. Halliday, M. Lauricella, S. Lishchuk, G. Pontrelli, T. Spencer, and S. Succi, Multicomponent Lattice Boltzmann Models for Biological Applications, in *Numerical Methods and Advanced Simulation in Biomechanics and Biological Processes*, edited by M. Cerrolaza, S. J. Shefelbine and D. Garzón-Alvarado (Academic Press, Cambridge, Massachusetts, USA, 2018), pp. 357–370.
- [85] M. Geier, A. Greiner, and J. G. Korvink, Cascaded digital lattice Boltzmann automata for high Reynolds number flow, *Phys. Rev. E* **73**, 066705 (2006).
- [86] S. Mukherjee, P. Berghout, and H. E. Van den Akker, A lattice Boltzmann approach to surfactant-laden emulsions, *AIChE J.* **65**, 811 (2019).